Received: 20 September 2023 | Revised: 19 December 2023 | Accepted: 24 December 2023

DOI: 10.1111/ffe.14231

ORIGINAL ARTICLE

FFEMS Fatigue & Fracture of Engineering Materials & Structures WILEY

The role of peening processes as a pre-treatment to anodizing on fatigue behavior of aircraft aluminum alloy

G. Renna[1] | M. A. Attolico[2] | V. Moramarco[2] | C. Casavola[2]

[1]Department of Engineering for Innovation, University of Salento, Lecce, Italy

[2]Department of Mechanics, Mathematics and Management, Polytechnic University of Bari, Bari, Italy

Correspondence
M. A. Attolico, Department of Mechanics, Mathematics and Management, Polytechnic University of Bari, Via Orabona 4, 70125 Bari, Italy.
Email: micheleangelo.attolico@poliba.it

Abstract

In this work, the possibility of employing shot peening and laser peening as pre-treatments to a tartaric–sulfuric anodizing process on the fatigue behavior of 7050-T7451 aluminum alloy components was investigated. The surface modifications and stress fields induced by the combination of the peening and anodizing processes were evaluated by scanning electron microscopy and residual stress assessment methodologies based on diffraction techniques, respectively. It was found that the anodizing process alone results in a significant reduction in fatigue life compared to the as-machined condition especially in the high-cycle fatigue (HCF) region of the *S–N* diagrams due to the presence of defects within the anodic layer that act as stress concentrators facilitating the initiation of fatigue cracks. The application of both shot and laser peening treatments is demonstrated to offset the negative effects induced by anodizing, offering greater safety margins useful for the design of critical aeronautical structures.

KEYWORDS

aluminum alloys, electron microscopy, fatigue, laser methods, stress/strain measurements, surface phenomena, X-ray analysis

Highlights

- The possibility to employ peening processes as pre-treatments to anodizing was studied.
- No significant influence of anodizing on residual surface stresses was observed.
- SP and LP provide significant benefits in the fatigue behavior of anodized components.
- Thicker anodic layers result in greater susceptibility to fatigue crack nucleation.

Abbreviations: 4PB, four-point bending; HCF, high-cycle fatigue; LCF, low-cycle fatigue; LP, laser shock peening; SEM, scanning electron microscopy; SP, shot peening; TSA, tartaric–sulfuric acid; XRD, X-ray diffraction.

1 | INTRODUCTION

The 7xxx series aluminum alloys (Al–Zn–Mg–Cu system) are widely used in aeronautical applications. Their high strength-to-weight ratio makes them ideal candidates for structural components or highly stressed parts, especially when the main requirement is fatigue strength. However, the difference in electrochemical potential between the secondary phases formed by alloying elements and the aluminum matrix often results in a reduction in the corrosion resistance of aluminum alloys, thus making it necessary in the use of specific surface treatments aimed at providing additional corrosion protection.[1,2] The oxide layer that naturally forms on the surface of aluminum components when they are exposed to air is not sufficient to ensure adequate corrosion resistance for the severe service conditions of aerospace environments, characterized by high-temperature gradients and the presence of different chemical agents.[3]

Nowadays, the anodizing process is commonly used to enhance the corrosion protection properties of base material in aerospace applications: An artificial stable oxide layer is generated on the treated surface of the part to ensure appropriate resistance against corrosive agents. Depending on the choice of anodizing voltage and time, chemical composition, and electrolyte temperature, the dimension of the anodic barrier can vary from a few micrometers up to several millimeters, with a different impact on the overall mechanical behavior of the part.[4] In particular, it has been widely demonstrated in the scientific literature that the presence of the anodic layer has a significant influence on the fatigue behavior of materials, and this was attributed mainly to the following reasons: firstly, the brittleness and the presence of porosity that easily cracks under cyclic tensile loading and the strong adhesion of the anodic layer to the substrate; secondly, the occurrence of tensile residual stresses due to the elastic incompatibility between the anodic layer and the base material surface; and lastly, the formation of pit-like defects that could act as preferential sites for the nucleation of fatigue cracks.[5–15]

From a structural point of view, it is crucial to ensure both corrosion resistance and fatigue properties in components. To achieve this, the anodizing process must be optimized to meet design requirements regarding the thickness and morphology of the anodic layer. Consequently, low anodic coating thicknesses, typically ranging from 2 to 7 μm, are utilized. This range allows for an excellent compromise between fatigue resistance and corrosion protection, fulfilling the specific needs of aerospace applications. For decades, chromic acid was the optimal choice for aeronautical applications because of the optimal physical and chemical characteristics of the anodic layer. Nevertheless, due to the toxic and carcinogenic nature of hexavalent chromium compounds,[16] the European Union has set stringent restrictions on the production and use of these compounds, which prompted the search for new and ecological anodizing solutions capable of guaranteeing similar physical, chemical, and mechanical properties.[17–20] The most widely used processes as an alternative to chromic anodizing are sulfuric, tartaric, tartaric–sulfuric, and phosphoric acid anodizing. Numerous studies in the scientific literature have extensively investigated these processes, aiming to provide comprehensive information regarding the morphology of the anodic layer and the effects induced by its presence on the physical and mechanical properties of the material. In particular, the anodizing in tartaric–sulfuric acid (TSA) solution is an electrochemical process, recently developed by Airbus, which favors the growth of an anodic barrier layer characterized by corrosion properties comparable to those obtained by chromic anodizing.[3,4,21,22] However, little information has been provided on the effects of the presence of the TSA anodic layer on the fatigue behavior of the treated components.[23–25]

To balance the negative effects of anodizing on the fatigue resistance of structural parts in the high-cycle regime and at the same time guarantee the high mechanical performance required in the aeronautical field, it is possible to adopt specific surface engineering processes before anodizing, such as peening processes, capable of locally introducing residual compressive stress fields to slow down the propagation of fatigue cracks or even prevent their nucleation.[26–28] In order for such processes to provide the required increase in fatigue life, the induced residual stress field must possess certain characteristics, such as an adequate depth of penetration, a predetermined depth and intensity of the residual stress peak, and a well-defined trend reversal point. Achieving these characteristics typically requires careful design and control of the peening process.[29–33] In addition, a thorough analysis of the surface integrity and morphological and microstructural properties of the component following the peening process is essential to ascertain the absence of factors, such as high surface roughness or the presence of superficial flaws, which may hurt the fatigue properties of the material.[34–38]

In this work, the possibility of using laser shock peening (LP) and shot peening (SP) as a pre-treatment to anodizing will be verified to compensate for the decrease in fatigue properties caused by the presence of the anodic layer. For this purpose, both a study of the residual stress field and a surface morphology analysis of the specimens in different conditions will be performed. Moreover, the results of fatigue tests conducted on prismatic bending bars ($K_t = 1$) in untreated, anodized, and peened–

anodized conditions will be proposed and discussed. Finally, a study of the morphological characteristics of the specimens under the different conditions analyzed and a fractographic analysis following the fatigue tests were proposed.

2 | MATERIALS AND METHODS

2.1 | Material and size of test samples

Aluminum alloy 7050-T7451, whose mechanical properties are shown in Table 1, was used in this work.[39] The wt% composition of 7050 alloy consists of 2.3 Cu, 6.2 Zn, 2.25 Mg, 0.12 Si, 0.1 Zr, 0.15 Fe, ≤0.04 Cr, ≤0.10 Mn, and 0.06 Ti, as defined in the material data sheet.

Fatigue samples were taken from a laminated plate making sure that the main axis of the specimens coincided with the lamination direction of the plate. The shape and dimensions of the specimens are established by the reference standard EN 6072:2016 and are shown in Figure 1A for completeness.[40]

Fatigue tests were carried out on four different groups of specimens, distinguished by their different surface conditions: as-machined specimens (untreated specimens), specimens subjected only to the TSA anodizing process (An. specimens), specimens subjected in series to mechanical SP and TSA anodizing treatments (SP + An. specimens), and finally, specimens subjected to LP and TSA anodizing treatments (LP + An. specimens).

Based on this classification, it will be possible to analyze individually the influence of the anodizing process when applied to the base material as well as to evaluate the effectiveness of the laser peening process when used as a pre-treatment to anodizing, comparing the relative mechanical performance with that derived from an established process in the aircraft industry such as SP.

TABLE 1 Mechanical properties of 7050-T7451 aluminum alloy.[39]

σ_{yield} (MPa)	σ_{UTS} (MPa)	Ductility (%)	E (GPa)	ν
469	524	11	71.7	0.33

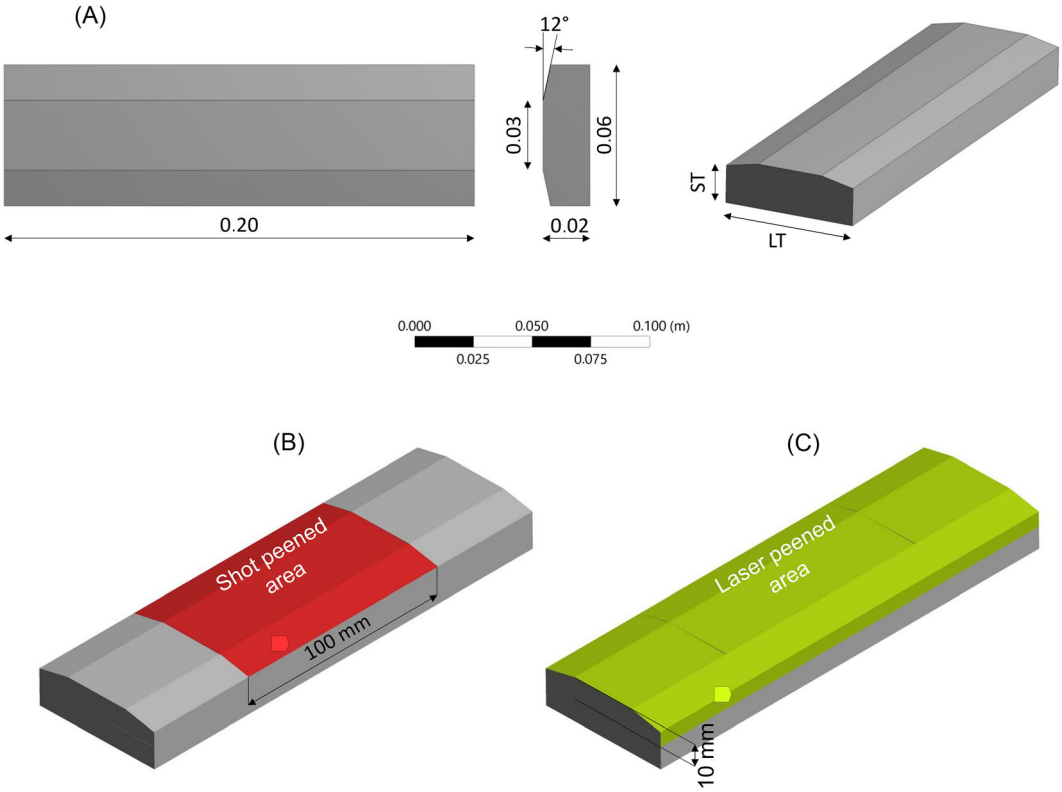

FIGURE 1 (A) Shape and dimensions of fatigue specimens (all dimensions are in meters). Identification of regions subjected to different peening processes: (B) region subjected to shot peening (highlighted in red) and (C) region subjected to laser peening (highlighted in green). [Colour figure can be viewed at wileyonlinelibrary.com]

2.2 | Anodization in TSA solution

The samples were initially treated using an alkaline detergent to remove organic and inorganic dirt deposits and process residues; in a second step, they were subjected to a pickling process in acid solution (HNO_3, H_2SO_4, and $Fe_2(SO_4)_3(H_2O)_n$) to promote the growth of a well-adhered and uniform oxide barrier. The actual anodizing was conducted inside an electrolytic bath consisting of 80 g/L $C_4H_6O_4$ and 40 g/L H_2SO_4 maintained at an average temperature of 40°C and applying a potential difference of 13–15 V for 22 min in the case of An. and SP + An. specimens and 45 min in the case of LP + An. specimens. As a consequence of the different treatment times, the anodic layer of the LP + An. specimens will be about twice the thickness of the anodic layer of the An. and SP + An. specimens. The different anodizing time chosen for the LP + An. specimens is due to the intention to verify whether the LP process can still provide fatigue performance comparable to that offered by SP despite the increased thickness of the TSA layer.

2.3 | SP process

Both mechanical and laser peening processes were carried out before the TSA anodizing treatment. The SP treatment was applied in the central portion of the specimen surface subjected to tensile stress according to four-point bending (4PB) load configuration (Figure 1B). The specimens were initially shot peened to full coverage using cast steel shots with an average size of 600 μm at an intensity of 0.20–0.24 mmA. Next, the specimens were subjected to a decontamination process using glass shots of smaller size (300 μm) and with a resulting intensity of 0.26–0.32 mmN.

2.4 | LP process

Laser peening treatment was applied on the entire tensile surface and part of the side surfaces of the fatigue specimen, as shown in Figure 1C. A Nd:YLF laser system ($\lambda = 1053$ nm) operating at a pulse frequency of 10 Hz was employed. The treated surface was preliminarily covered with a layer of ablative material (aluminum tape) in order to promote the formation of the plasma cloud, and a laminar stream of water was used to confine the plasma expansion by directing it toward the thickness of the sample. Laser pulses with a nominal energy of 2.5 J and duration of 20 ns were then projected through a circular spot of 2 mm diameter according to a predefined pattern to ensure complete coverage of the treated region.[29] Specifically, adjacent spots have an overlap rate of 33% in both the scanning and stepping directions to ensure complete coverage and uniformity of the induced residual strain field. The scanning and stepping directions correspond with the transverse and axial directions of the fatigue specimen, respectively. In addition, three different laser peening layers with a 33% phase shift between them in both main directions of the peening pattern were adopted.

2.5 | Residual stresses and microhardness measurements

An initial characterization of the residual stresses induced by the anodizing and peening processes on the surface of treated samples was carried out by X-ray diffraction (XRD) technique in accordance with the indications given in the reference standard UNI EN 15305.[41] Specifically, X-rays were generated by means of a chromium tube and projected onto the surface of the parts through a 2 mm diameter circular aperture collimator. The sin2Ψ technique was used for the evaluation of residual stresses. Eleven ψ tilt angles evenly distributed in the angular range (−45°, 45°) were used to compute elastic strain values in each direction. The diffraction angle (2θ) was set equal to 139.3°, and an exposure time of 40 s was selected. Measurements were based on the (peak hkl: 311) diffraction reflection of Kα radiation assuming the elastic constants S_1 and $S_2/2$ equal to respectively 1.905×10^{-6} and -4.887×10^{-6} MPa^{-1}.

Surface residual stresses were evaluated for each type of specimen at three points located on the longitudinal axis of the tensile surface of the fatigue specimens. Biaxial stress measurements were made along the longitudinal (σ_x) and transverse directions (σ_y) of the test samples.

An LP + An. specimen was randomly selected to verify the depth distribution of the residual stress field induced by the simultaneous application of the laser peening process and TSA anodizing treatment. The measurement was made at the midpoint of the tensile surface of the fatigue specimen up to a depth of about 1.75 mm from the component surface along both the evaluation directions. The analysis was conducted by removing layers of materials through a step-by-step electrolytic-polishing procedure (60 V for 5 s intervals) using Movipol-3 equipment (Struers) and an A2 electrolyte. Different removal steps were used depending on the depth of evaluation: 10 μm of removal up to a depth of 50 μm, 25 μm at depths between 50 and 200 μm, 50 μm between 200 and 500 μm, 100 μm between 500 and 1000 μm, and 250 μm between 1000 and 1750 μm. The XRD measurement parameters adopted for the

evaluation of surface residual stresses were similarly employed for in-depth measurements.

Vickers micro-hardness measurements were made according to ASTM E384 specification in the cross-section of untreated, SP + An., and LP + An. specimens. The indentations were performed applying a load of 100 g for 15 s using Shimadzu HMV-G2 type micro-hardness tester. Micro-hardness measurements were acquired at 15 different depths from the surface of the part spaced 100 μm apart.

2.6 | Fatigue tests

Fatigue tests were carried out on a Schenk PC 400M servohydraulic load frame equipped with a 250 kN load cell. The loading system consists of two structural steel beams connected to the grasping systems by bolted flanges. Two V-shaped grooves per beam served as seats for the support and load rollers, whose correct positioning relative to the specimen is ensured by the presence of guides that allow the supports to slide in the longitudinal direction. The rollers are free to rotate about their main axis during load application. In accordance with the reference standard EN 6072:2010[40] in relation to bending fatigue tests on flat specimens, the support and load rollers are positioned at a distance of 30 and 85 mm from the centerline of the sample, respectively (Figure 2).

The constant amplitude load signal was characterized by stress ratio of 0.1 and was applied at a steady-state frequency of 15 Hz. The tests were considered completed when the specimen completely failed or reached a predetermined number of cycles, that is, 3 million cycles, in the absence of visible fatigue cracks.

2.7 | Surface morphology analysis and fractography

The Zeiss EVO-MA10 scanning electron microscope was employed for analysis of two critical aspects: the surface morphology along the longitudinal section of the specimens and an in-depth investigation of the fracture surfaces. The microstructural analysis of substrate (base material) was conducted using an optical microscope following grinding and mechanical polishing. Specifically, the grain structure of substrate was revealed by etching with Keller's reagent (1 mL HF, 1.5 mL HCl, 2.5 mL HNO_3, and 95 mL H_2O). Specimen defect analysis was conducted using ImageJ software. Specifically, the percentage of defects was calculated as the ratio between the sum of the defect areas and the total surface examined. This evaluation was performed on three high-resolution scanning electron microscopy (SEM) images, randomly selected from the surface of the samples.

Fracture surfaces were instead analyzed to pinpoint the root cause of fractures, like cracks, and comprehend the mechanisms governing their propagation. Roughness profiles were obtained by means of a portable profilometer (MarSurf PS 10) equipped with a tip radius of 2 μm adopting an evaluation length of 15 mm, a cutoff length of 0.8 mm, head movement speed of 11 mm/s, and a maximum measurement range of 350 μm. Three measurements were taken for each major direction (longitudinal and transverse) of the prismatic specimens at randomly chosen positions on the surface subjected to tensile stresses in the 4PB fatigue test configuration to allow a more reliable statistical analysis of the results.

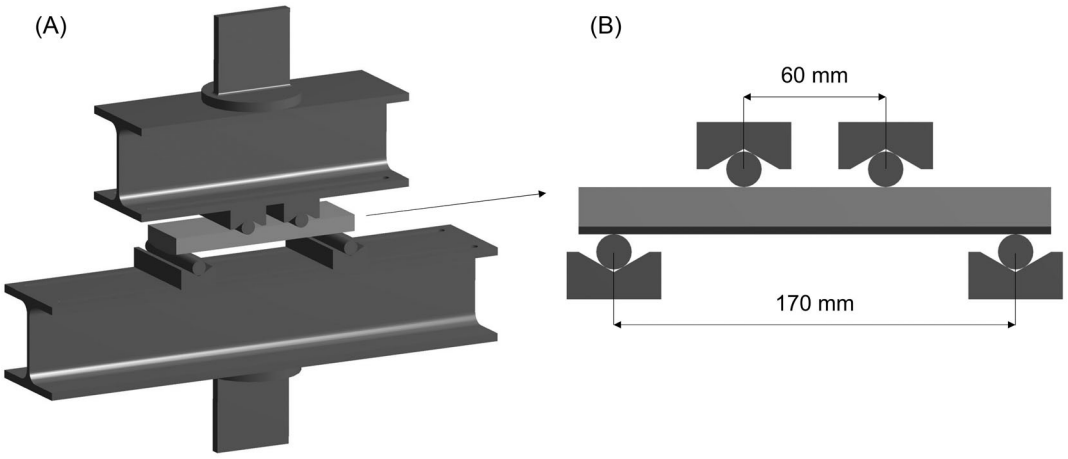

FIGURE 2 (A) Loading system for four-point bending fatigue tests. (B) Detail on the positioning of the loading and support rollers.

3 | RESULTS AND DISCUSSION

The microstructure of 7050-T7451 base material on the short transverse–long transverse (ST–LT) plane is shown in Figure 3. The T7451 treatment is performed specifically to achieve a proper combination of mechanical and physical properties in the 7050 Al alloy. It is commonly used in applications where these properties are crucial, such as aerospace components, structural parts, and high-performance equipment. The micrographs depicted in Figure 3A,B reveal a partially recrystallized microstructure characterized by equiaxed fine grains within larger grains. Particularly, it is possible to observe that both the constituent intermetallic particles and the grain boundaries are elongated along the rolling direction, assuming the typical flat pancake-shaped structure.

3.1 | Surface morphological changes

Figure 4A–F shows the SEM micrographs at low and high magnification of the top surfaces of as-machined, simply anodized, shot peened, and laser peened specimens. Untreated specimens show a uniform morphology characterized by the presence of limited surface defects, mainly in the form of chippings, presumably associated with the mechanical machining to which the sample was subjected before the anodizing process (Figure 4A,B). The average surface roughness of the examined surface shows values between 0.2 and 0.3 μm. More interesting, the TSA anodizing strongly affects the surface morphology of the sample: The surface appears less uniform than that of untreated specimens due to the presence of numerous defects in the form of micro-pores and cavities non-uniformly distributed on the specimen surface. In general, the size of typical micro-pores is less than 25 μm (Figure 4C). Additionally, it is possible to observe in the SEM micrograph (Figure 4D) that, in some areas, the micro-pores tend to group together forming isolated clusters of pores as large as 50 μm, which are significant from a structural point of view as preferred candidates as nucleation sites for fatigue cracks. The presence of these defects in the anodic layer has also been documented in several studies,[11,12,19] and it was demonstrated to have an inherently detrimental influence on fatigue resistance. As reported in the literature, these micro-pores increase the susceptibility of the anodic film to crack initiation and propagation, ultimately resulting in premature failure when subjected to cyclic loading conditions. In the anodizing process, micro-pores and cavities formation is associated with the high reactivity of intermetallic particles and secondary phases in the microstructure (especially compounds of zinc, magnesium, and copper in 7xxx series aluminum alloys) and inter-granular precipitates.

The density of defects of An. specimen, defined as the ratio of the total defect areas over the entire area examined, is less than 3%.

On the other hand, SEM analysis of the specimens subjected to the two peening processes (Figure 4E,F for the SP + An. and Figure 4G,H for the LP + An. specimens) shows that these processes influence the morphology in a different way.

In particular, the surface of the SP specimens exhibits the typical indentations (Figure 4E,F) generated by the collision of glass spheres on the surface during the decontamination phase of the SP process. The TSA layer develops on this starting morphology and leads to the formation of a final rough surface with micro-pores and voids similar in type, density, and size to those found in the case of simply anodized sample (Figure 4F). Instead, in the case of LP + An. samples, the specimen surface does not show the presence of visible indentations as in the case of SP specimen (cf. Figure 4E with Figure 4G). This is due both to the systematic nature of the LP

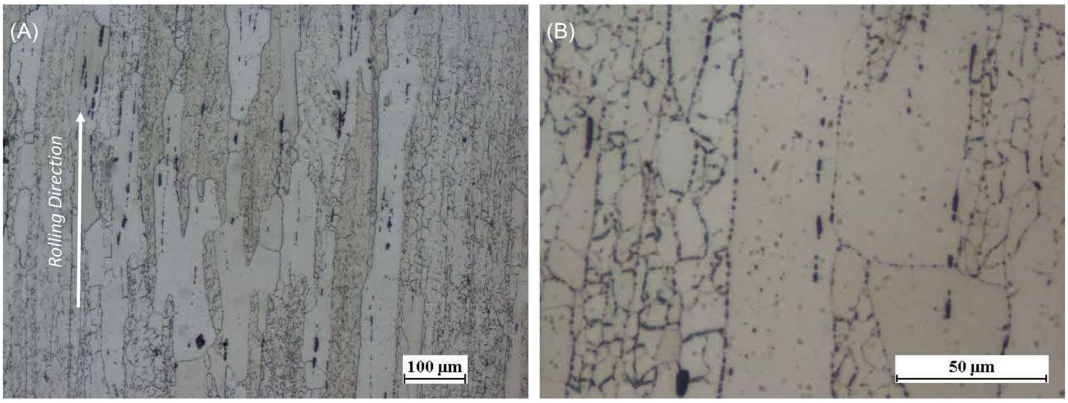

FIGURE 3 (A) Microstructure of 7050-T7451 untreated material on the ST–LT sectionplane. (B) Higher magnification view of intermetallic particles and grain boundaries.

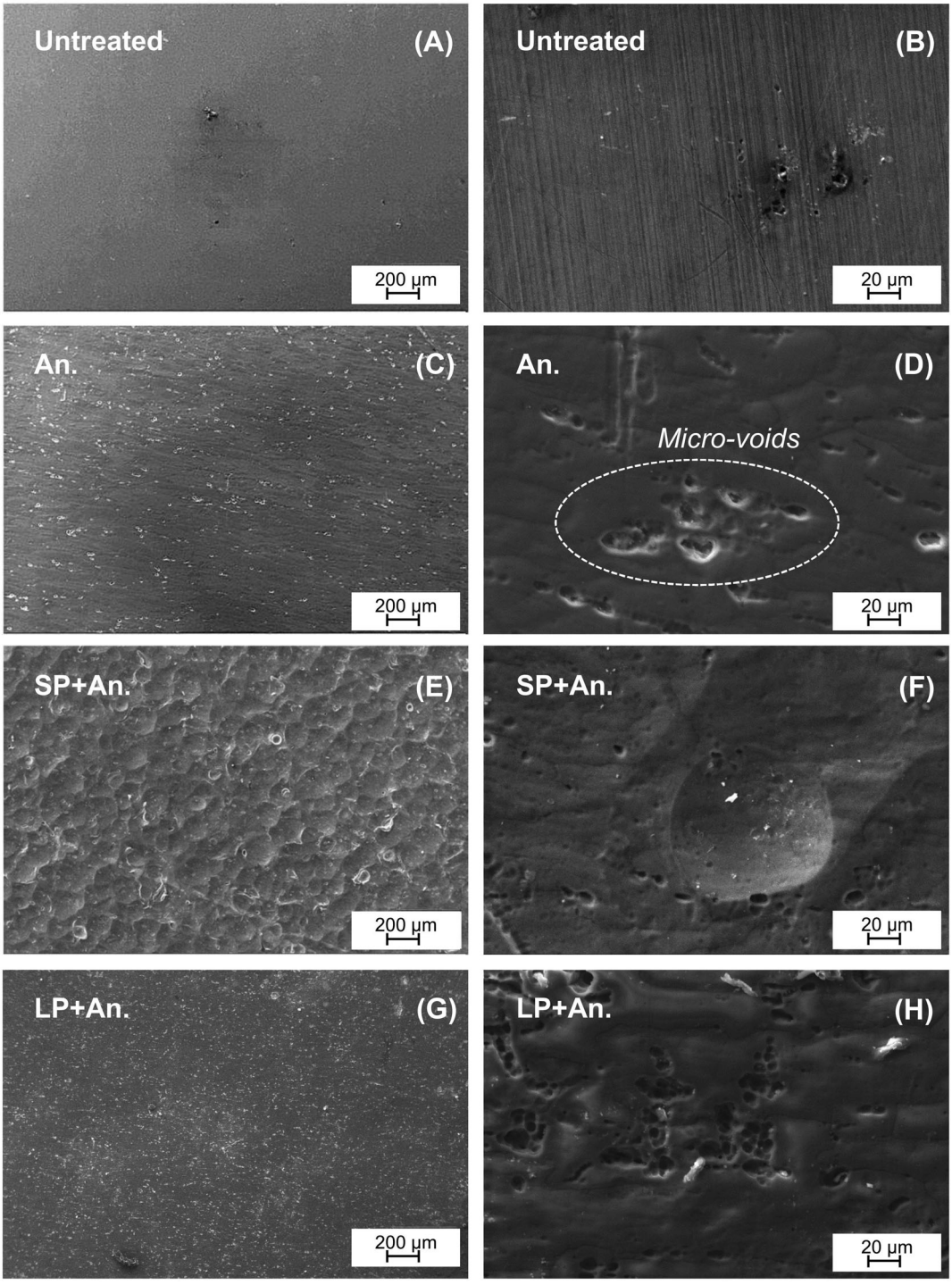

FIGURE 4 Top view (A–H) SEM micrographs (longitudinal–long transverse plane) at different magnifications: (A, B) of base material, (C, D) of the simply anodized component, (E, F) shot peened, and (G, H) laser peened together with TSA anodizing. Note in (B) detail of the defects on the surface of base material and in (D) micro-pores on the surface of the anodic layer.

process (ordered pattern of laser spots) as opposed to the randomness of impacts in the SP process and to the different size of the laser spots as compared to the physical dimension of the shots commonly used during mechanical peening. As a result, the surface appears similar to that of a simply TSA anodized specimens rather than that of an SP + An. specimens.

The different surface impact of the anodizing treatment and the SP and LP processes so far analyzed can be quantitatively evaluated by analyzing the roughness

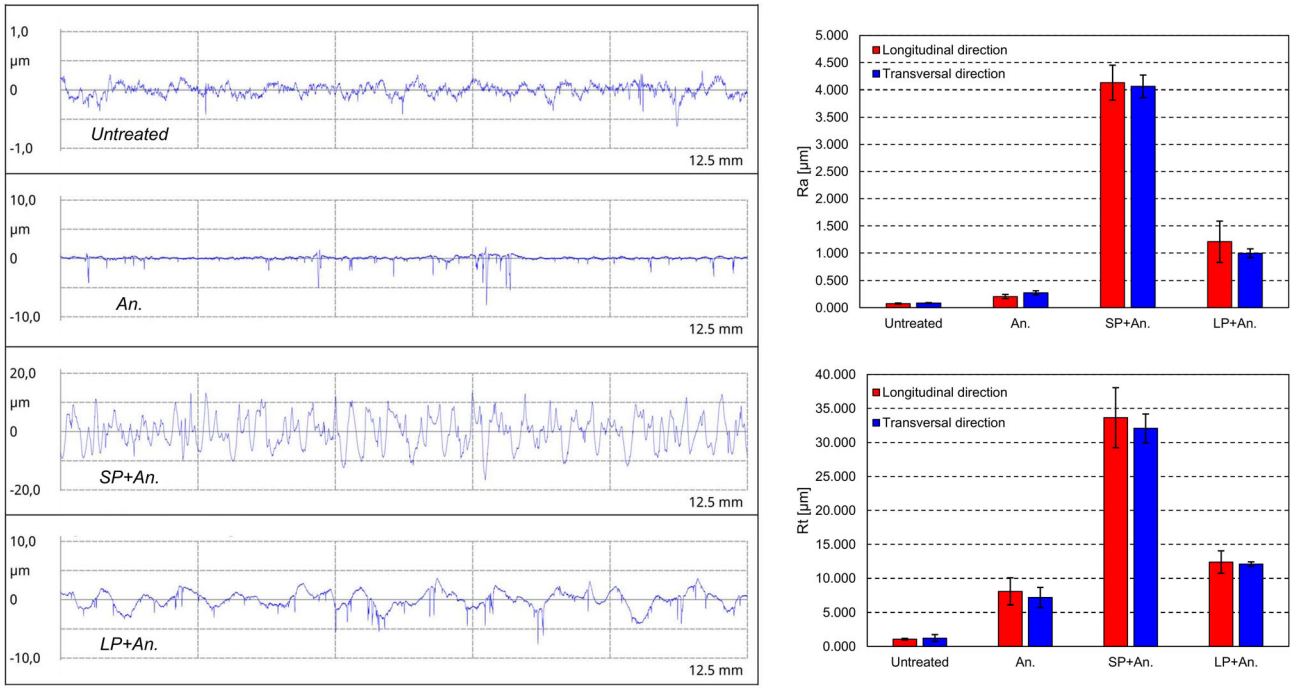

FIGURE 5 Typical roughness profiles and average values of the R_a and R_z roughness parameters of untreated, An., SP + An., and LP + An. specimens. [Colour figure can be viewed at wileyonlinelibrary.com]

profiles of the four categories of specimens considered and extrapolating the average roughness average (R_a) and mean roughness depth (R_z) values as defined by ISO 4287 standard. As evident from the roughness profiles and diagrams shown in Figure 5, the anodizing process induces a slight increase in roughness parameters in both evaluation directions compared to the untreated material due to the growth and inhomogeneity of the anodic layer on the component surface. In contrast, the LP process and particularly the SP process result in a significant increase in the R_a and R_z values as a consequence of the high plastic deformation to which the material surface is subjected as a result of the expansion of elastic waves (LP) or the impact of shots (SP). In particular, as emerged from the analysis of the SEM surface micrographs, the SP process determines roughness values more than twice higher than those typical of the LP process.

The type and size of the defects present on the anodic layer of the specimen subjected to the LP pre-treatment are comparable to that observed in the case of anodized and SP + An. specimens. However, the key difference lies in the density of these defects, which is significantly higher in the LP-treated specimen compared to the untreated and SP + An. specimens. In particular, the LP + An. specimen is characterized by a defect density of about 25%. This increase in the percentage of defects can be attributed to the longer anodization time compared to the other two class of specimens. Furthermore, as a result of using the double anodization time, an almost double thickness of the anodic film was observed (4.16 ± 0.47 µm) (Figure 6C,F) compared to that measured for An. (2.16 ± 0.4 µm) and SP + An. (2.08 ± 0.3 µm) specimens (Figure 6A,D and 6B,C). As expected, the thickness of two specimens An. and SP + An. was similar due to the use of the same anodizing time. The result obtained aligns with the existing literature for the given experimental conditions. For example, Lonyuk et al.[42] demonstrate that an increase in the thickness of the anodic layer results in a higher probability of developing defects and a tendency for less adhesion between substrate and oxide. These defects can include voids and cracks, which act as stress concentration points during cyclic loading favoring fatigue failure.

In order to better evaluate both the surface deformations induced by the SP and LP processes and the characteristics of the anodic barrier obtained by the anodizing process, the cross-section of the An. (Figure 6A,D), SP + An. (Figure 6B,E), and LP + An. (Figure 6C,F) specimens was analyzed by SEM. From a careful analysis of the interface between the anodic layer and the substrate, it was observed that the anodic layer appears uniform, compact, and well adhered to the aluminum substrate. Moreover, the anodic layer takes the shape, contours, and surface characteristics of the specimen. This suggests that during the anodic oxidation process, the anodic film has grown and developed in a way that mirrors the

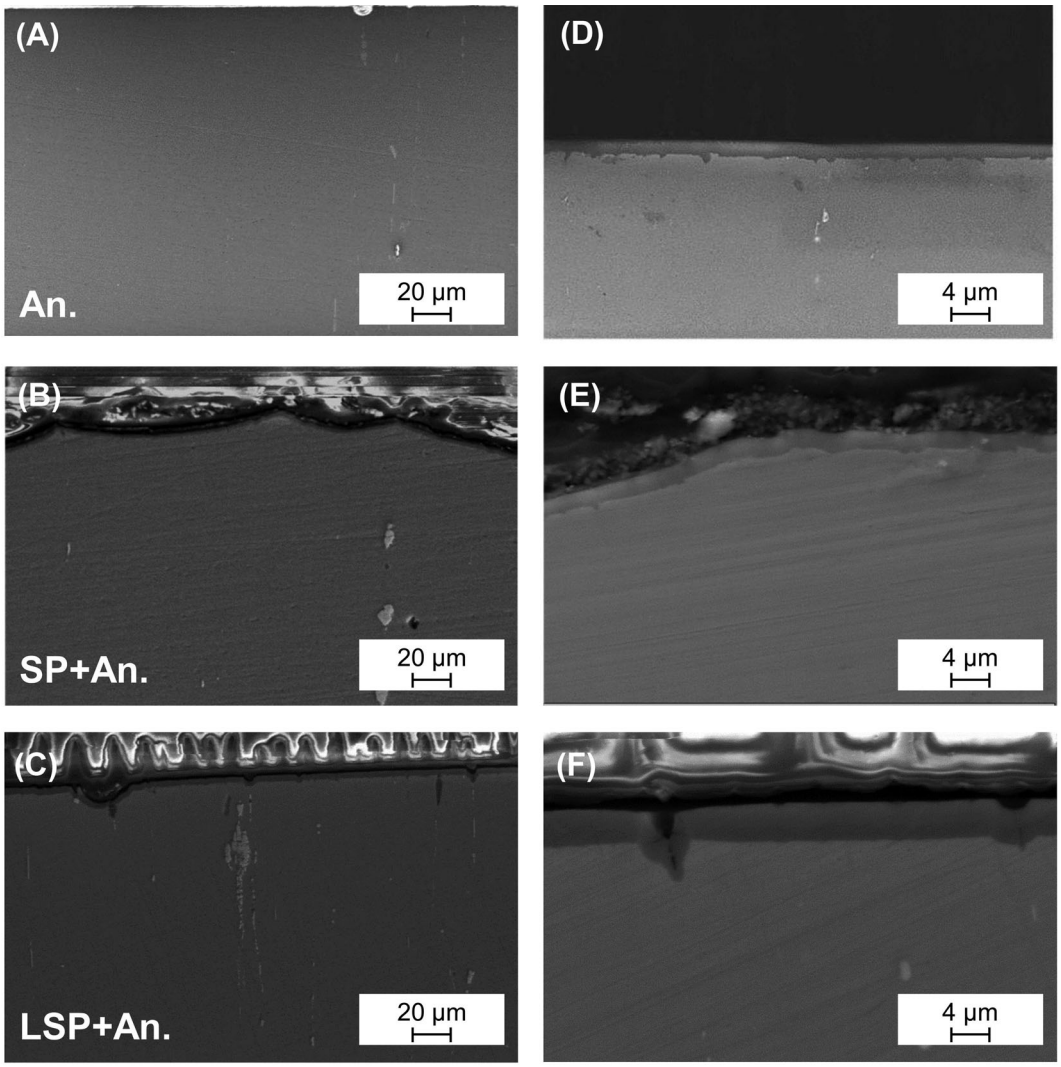

FIGURE 6 SEM micrograph of the LT–ST plane of (A, D) An., (B, E) SP + An., and (C, F) LP + An. components at different magnifications.

topography of the substrate. In other words, the anodic layer has followed the contours and irregularities of the specimen's surface, creating a replica or a representation of the surface features in the resulting anodic film.

Also in the case of SP + An. specimen, a good adhesion between the anodic layer and the material substrate is observed, despite the higher roughness average values induced by mechanical peening (Figure 6B,C). Moreover, it is interesting to note that some micro-cracks generally less than 25 μm in length are observed originating on the top of the oxide layer and propagating through the substrate of LP + An. samples (Figure 6F).

The plastic deformation mechanism induced by peening processes was also evaluated through micro-hardness indentations. The micro-hardness profiles of the untreated, SP + An., and LP + An. specimens are shown in Figure 7. It was found that the untreated specimen is characterized by an average micro-hardness value of 158 ± 1 HV. From the comparison between the micro-

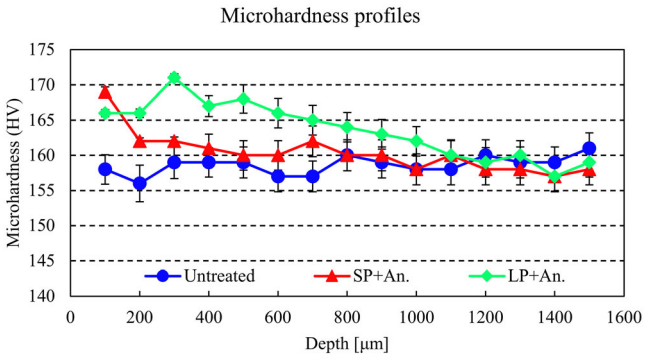

FIGURE 7 Micro-hardness profile ($HV_{0.1/15}$) of untreated, SP + An., and LP + An. samples. [Colour figure can be viewed at wileyonlinelibrary.com]

hardness profiles shown in Figure 7, a variation of the surface state introduced by the SP and LP processes emerged. This variation can be observed both in terms of

the maximum hardness value achieved, with which a level of hardening can be associated, and in terms of effective thickness, representative of the volume of material affected by plastic deformation. In particular, the SP + An. specimen exhibits a peak of micro-hardness of 169 HV at a depth of 100 μm and a subsequent gradual descent until typical hardness values of the base material are reached at a depth of 500 μm. Therefore, SP induces a significant amount of plastic deformation on the surface while achieving a moderate compressive depth of approximately 0.4 mm. Conversely, LP process generates a comparable magnitude of surface stress as SP but offers a significantly greater depth of penetration of about 1.1 mm. In particular, it can be observed that the LP + An. sample presents a hardness peak at a depth of 300 μm (171 HV). In other words, based on the microhardness profiles, it is possible to hypothesize a greater improvement in fatigue of the LP pre-treated specimens compared to the SP ones. This is because LP pretreatment affects a much larger region of material (a greater extent of the hardened region) while maintaining a similar magnitude of stress on the surface. The increased depth of penetration can improve the material's resistance to fatigue and enhance its overall performance.

It is important to point out the small difference between the hardness values of peened samples processes compared with the base material. This phenomenon was already discussed in the scientific literature and predicts little influence of the peening processes on the hardness of peak aged aluminum alloys, such as 7050-T7451 aluminum alloy.[43]

3.2 | Residual stress analysis

The values assumed by residual stresses in the axial and transverse directions at the three measurement points on the tensile surface of the fatigue specimens are shown in Figure 8. The data were obtained by averaging the results of residual stresses measured on a batch of four specimens in each group. Linear interpolation functions were used to evaluate the trend of axial and transverse residual stresses as the measurement position on the specimen surface changed.

In agreement with the above results, compressive stress states of different magnitudes are observed in all four categories of specimens considered. As expected, the stresses are almost uniform on the surface of the specimen, with the sole exception of the untreated specimens that show slight nonuniformity of surface residual stress values, probably associated with the technological processes to which the component has been subjected. The untreated specimens exhibit a slight compressive tensional state (about −100 MPa) along both in axial and transverse directions. It is commonly reported that the anodizing process induces surface tensile stress states, as highlighted in several past scientific papers.[44–46] However, the analysis of the reported data shows a trend contrary to expectations, in which the anodizing process in tartaric–sulfuric solution appears to induce slight compression, in both the axial and transverse directions. It should be pointed out, however, that the extremely small thickness of the anodic layer causes residual stress measurements by X-ray diffractometry (penetration depth of about 10 μm) to be made on a volume of material that does not consist entirely of the anodic layer but rather largely of base material. As a result, the measured residual stresses will not exclusively reflect the stress state within the anodic layer but will also incorporate contributions from the underlying base material.

Much more interesting, however, is to analyze the results of specimens consecutively subjected to peening and anodizing processes. Regarding surface residual stresses of SP + An. samples, an average residual stress field of about −190 MPa is observed in both axial and transverse directions. The uniformity of stresses in the two measurement directions is a direct consequence of the stochastic nature of SP and the choice of appropriate coverage and intensity values.

Unlike the SP + An. specimens, the LP + An. specimens exhibit higher compressive surface residual stresses. On average, a value of about −250 MPa is observed along both the considered directions. The presence of compressive stress field on the surface of the specimen following LP treatment highlights the absence of local scorching, which was previously confirmed by visual inspection of the specimens (see Figure 4), while the uniformity of stresses in the two directions suggests that the overlapping strategy between adjacent laser spots and the offset interposed between consecutive layers favored the formation of a nearly equibiaxial stress state. The stress state intensity induced by LP process is in line with results published in other scientific papers concerning LP applications on aircraft aluminum alloys.[47,48]

To verify the compliance of the LP process with the design requirements, an in-depth residual stress profile was obtained from LP + An. by XRD technique. Figure 9 shows the trend of longitudinal measured at the midpoint of the laser peened region. This evaluation direction was chosen since it coincides with the main direction of loading resulting from the 4PB test configuration. The profile of in-depth residual stresses was interpolated using a cubic function. The resulting profile exhibits a peak stress intensity equal to approximately −350 MPa (corresponding to about 75% of the yield stress of the material) at about 0.4 mm from the

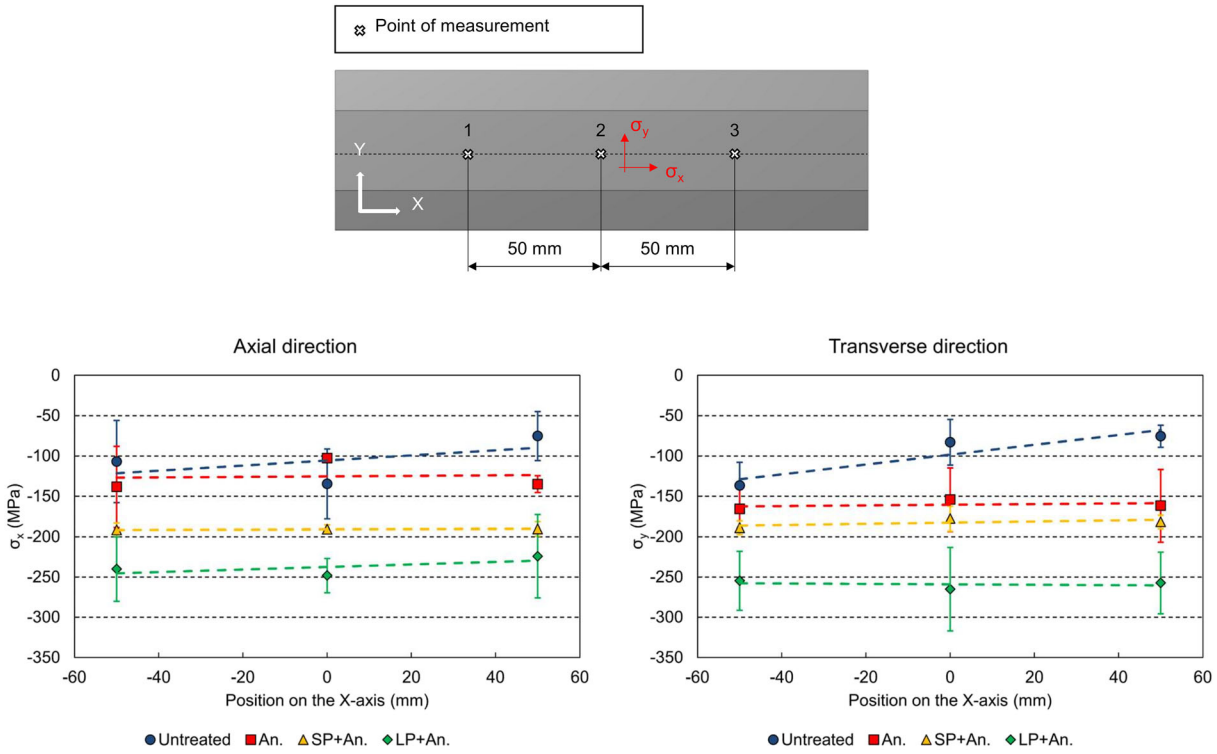

FIGURE 8 Residual stress values along the axial and transverse directions in three different positions on the surface of untreated, An., SP + An., and LP + An. specimens. [Colour figure can be viewed at wileyonlinelibrary.com]

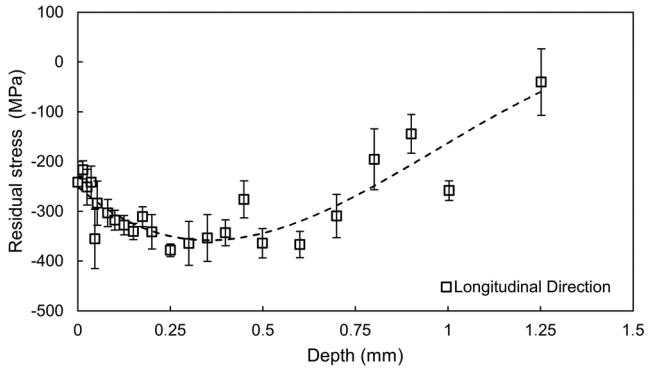

FIGURE 9 Trend of residual stresses as a function of measurement depth in LP + An. specimen.

surface and the presence of compressive stresses well beyond 1 mm depth.

3.3 | 4PB fatigue test results

The fatigue life of each specimen is represented on a semi-logarithmic plot as a function of the maximum value of the applied cyclic stress. The trend curves were obtained by interpolating the data according to indications reported in the ASTM E739-15 standard (Equation 1). All fatigue data were reported in Table S1.

$$Log\,N = A + B\,Log\,S \tag{1}$$

where N represents the fatigue cycles reached at stress level S, and A and B are fitting constants.

Fatigue results related to untreated and anodized specimens were taken from a previous study by the authors[25] and are reposted in order to provide a comprehensive discussion about the effects of anodizing treatment when employed alone and in combination with peening processes.

As expected, the analysis of the fatigue curves of untreated and An. specimens depicted in Figure 10 shows that the anodizing process determines a substantial reduction in the fatigue properties of the base material in the MCF and high-cycle fatigue (HCF) regions of the diagram, despite the limited dimension of the oxide layer.[25] The presence of the defects, such as voids and microcavities, significantly impacts the HCF performance of simply anodized components since the phenomenon of fatigue crack nucleation is predominant in this region compared to that of fatigue crack propagation. This is even more evident by comparing the trend of the two fatigue curves in the low-cycle fatigue (LCF) region: They show almost overlapping trends by virtue of local plasticity that tend to mitigate the stress state even in the presence of defects constituting stress concentration sites. Experimental results demonstrated that the anodizing

Fitting parameters	Untreated	An.	SP+An.	LP+An.
A	14.18	15.28	18.04	17.39
B	-3.61	-4.10	-4.94	-4.69

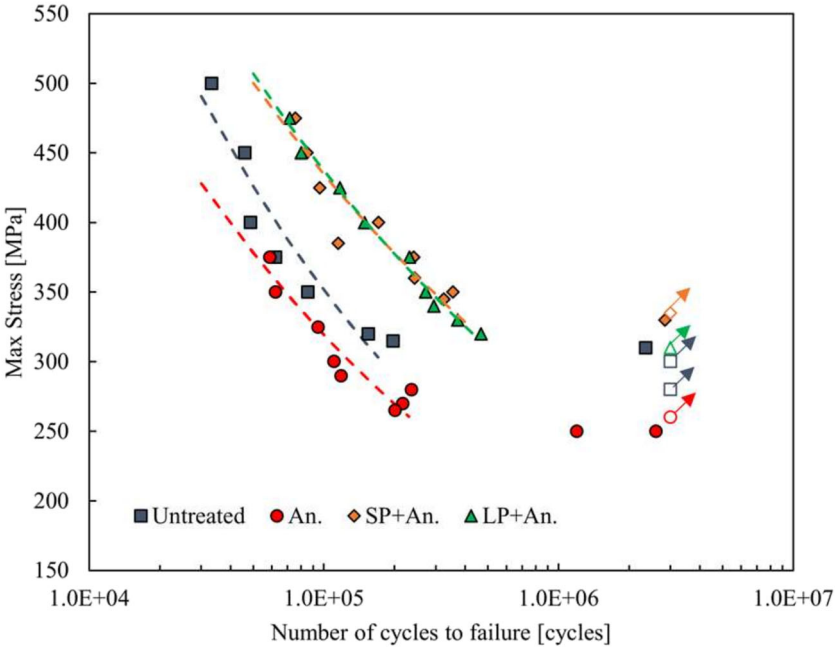

FIGURE 10 *S–N* curves of untreated, An., SP + An., and LP + An. specimens. Fatigue data related to untreated and anodized specimens were taken from a previous study by the authors.[25] [Colour figure can be viewed at wileyonlinelibrary.com]

process results in a fatigue limit reduction of about 15% compared to the value obtained from as-machined specimens. At 300 MPa, anodized samples show failure after about 110,000 cycles, while untreated components reach runout. In the scientific literature, the reduction of fatigue life in anodized samples is commonly linked to the presence of a residual tensile stress state induced by the development of an anodic layer generally thicker than 10 μm.[6,12,13,24] In the case under study, however, the limited thickness of the anodic layer (between 2 and 4 μm) had an almost negligible influence on the residual surface tensile state, as evidenced by the measurements analyzed in Section 3.2. Based on these considerations, the influence of any residual stress field caused by the anodizing process on fatigue behavior can be considered negligible.

The employment of SP and LP as pre-treatments to TSA anodizing certainly provides a significant increase in the fatigue properties. However, it is important to dwell carefully on the trend of the two fatigue curves, focusing on the different dimension of the oxide layer in the two different cases: In fact, LP + An. specimens have an anodic layer twice as thick as SP + An. specimens as a result of the different treatment time in TSA solution. In the LCF regime of the *S–N* diagram, the trends of the two fatigue curves of the SP + An. and LP + An. specimens exhibit almost coincident trends and very significant increases in fracture life compared to the untreated and An. specimens. Specifically, at 450 MPa, both the SP and the LP processes provide an increase in fatigue life of about 100% when compared with the base material and the simply anodized specimens, while at a maximum stress level of 375 MPa fatigue life more than three times higher than those of the untreated and An. samples are estimated in the shot and laser peened samples. The curve trends of the two groups of peened specimens vary in the transition region between the LCF regime and the MCF and HCF regimes. The SP + An. specimens exhibit an estimated fatigue limit 1.08 times higher than the LP + An. specimens. It must be noted that the fatigue limit of LP + An. specimens is almost coincident with that of untreated specimens. Thus, it seems evident that the presence of an anodic layer twice as thick as that on the SP + An. specimens causes a significant reduction in the performance in the HCF regime of the laser peened specimens. Despite the higher compressive surface stresses (see Figure 8) and greater stress penetration depth in LP compared to SP samples (see Figure 9), it can be supposed that the presence of surface micro-cracks observed in the cross-section of laser peened samples is responsible for the phenomenon of fatigue crack nucleation by acting as preferential sites of stress concentration. This is a

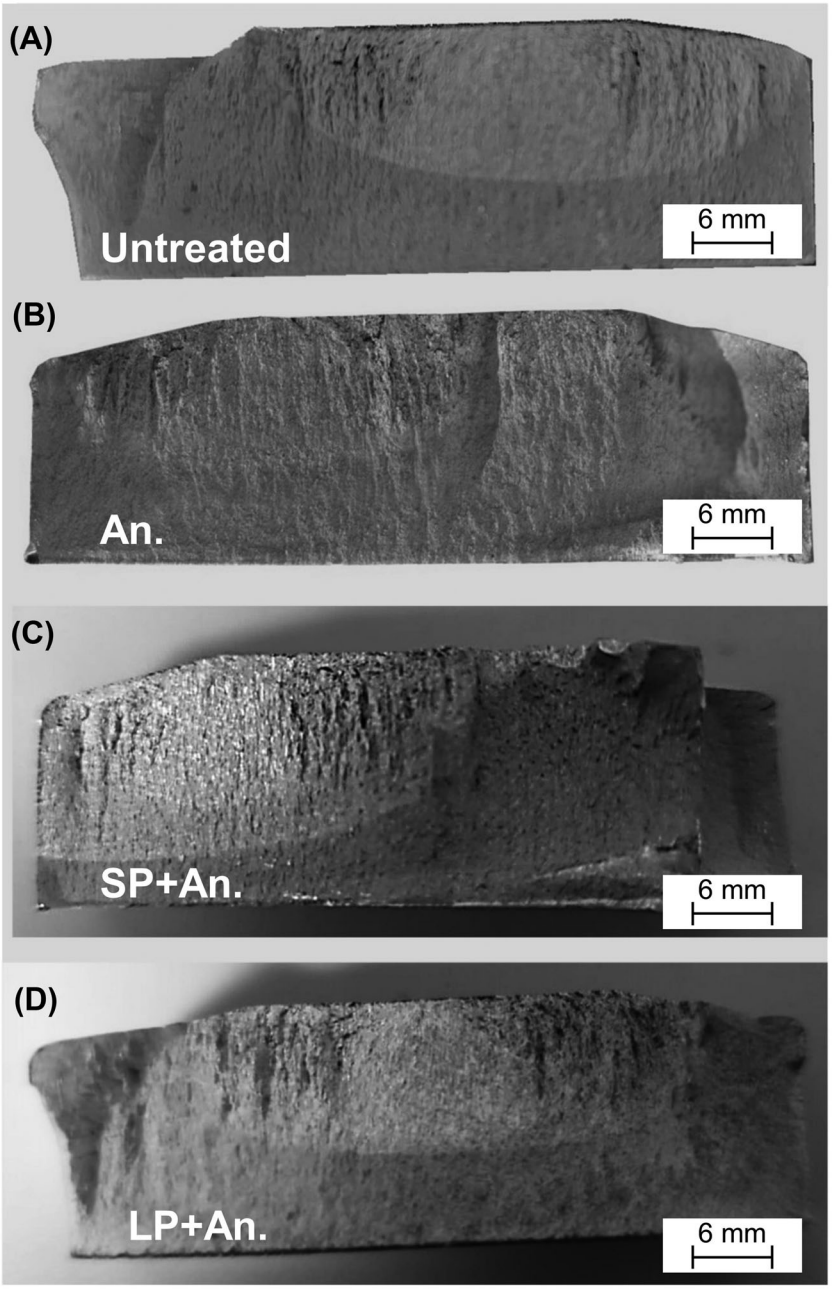

FIGURE 11 Overall view of the fracture surfaces in HCF regime of (A) untreated, (B) An., (C) SP + An., and (D) LP + An. specimens.

likely explanation because no appreciable differences in behavior are found in the LCF region of the fatigue curves of both shot and laser peened samples, a region in which local plasticization phenomena at the surface defects caused by anodization tend to attenuate and equalize the resulting maximum stress states ensuring comparable fatigue properties.

3.4 | Fatigue fracture surface analyses

To better analyze the mechanisms underlying crack nucleation and propagation phenomena, the fracture surfaces of samples that failed in the HCF zone of the fatigue curves were examined by SEM. In this regard, Figure 11 shows reconstructions of the fracture surfaces of the untreated, An., SP + An., and LP + An. specimens. From an initial analysis, it is apparent that the nucleation of fatigue cracks predominantly occurs on the surface for all examined specimens (Figure 12A–H). It can be clearly observed that fatigue crack propagates through an area characterized by distinct tear-ridges resembling river patterns (see the white dashed lines in Figure 12A,C,E,G). These patterns extend uniformly throughout the crack propagation area, culminating in the region of ultimate shear failure. Additionally, small

regions showing cleavage-like fractures can easily be observed along the edge of the fracture surfaces, as illustrated in Figure 12D,F,H.

More interesting, SEM analysis at higher magnifications revealed an important aspect: Fatigue cracks originate mainly in correspondence with defects present on the surface of the specimens. As demonstrated earlier in Section 3.1, the distinct morphological defects present arise from varied surface treatments. Specifically, it was observed that in the anodized specimen, the cracks

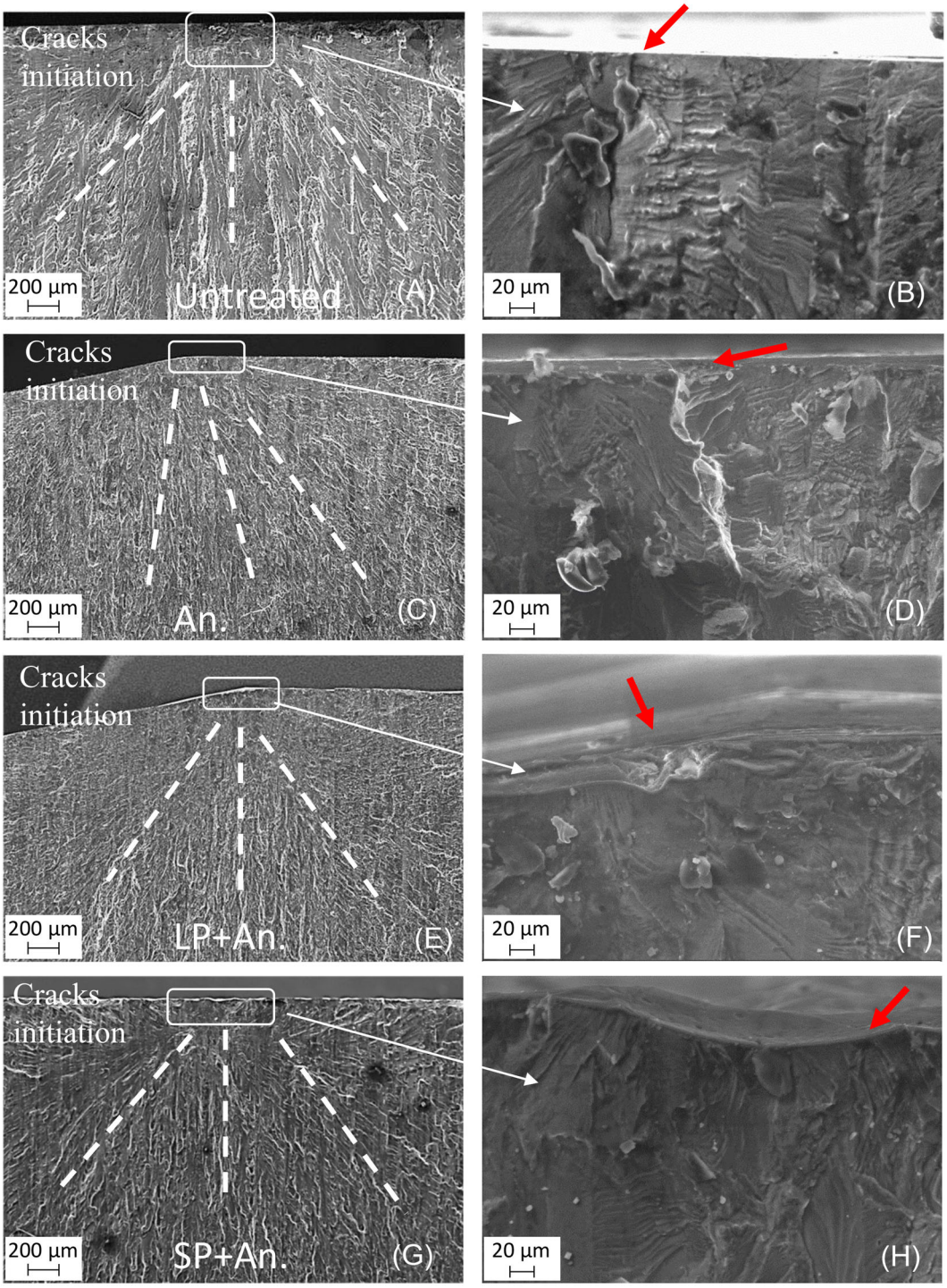

FIGURE 12 Enlarged details of component fracture surfaces: (A, C, E, G) SEM images of the fatigue crack nucleation regions for the untreated, An., LP + An., and SP + An. specimens, respectively; (B, D, F, H) detail of the crack initiation sites occurred on the surface for the untreated, An., LP + An., and SP + An. specimens, respectively. [Colour figure can be viewed at wileyonlinelibrary.com]

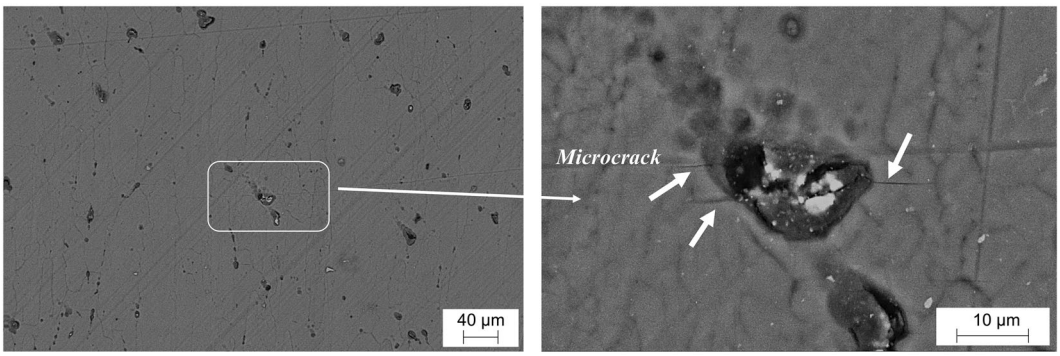

FIGURE 13 SEM micrograph of the front surface of an anodized sample following fatigue testing. Numerous non-propagating fatigue micro-cracks originating at surface defects are clearly visible.

originate at micro-voids or cavities present on the surface of the anodic layer induced by the TSA process (Figure 12D). Similar behavior was observed in the anodized specimens subjected to LP pre-treatment (Figure 12G). In fact, as revealed by Figure 13, these micro-voids in the anodic layer have a key role in the formation of fatigue micro-cracks, which eventually merge into a single crack front in the most advanced stages of propagation.

In contrast, in the case of the SP + An. specimens, the crack nucleation sites are predominantly located at geometric discontinuities, such as the valleys of roughness profiles. On the other hand, SP roughens the surface and consequently produces many small valleys that induced localized regions of stress concentration that can be likely considered as a cause of the reduction of the fatigue strength.

These latter observations are noteworthy considering the stress state of the pre-treated specimens (untreated and An.) discussed in Section 3.2. One would expect a shift in the crack nucleation point toward the subsurface region of the specimens (LP + An. and SP + An.) because of compressive residual stresses introduced by the peening processes. However, the 4PB load configuration results in maximum bending stresses occurring near the surface of the part. These stresses gradually decrease with depth and exhibit sign reversal at the neutral axis. Consequently, the surface remains the most stressed region (within a range of 1 mm from the surface), despite the superposition of compressive stresses caused by the pre-treatment processes. Moreover, stress concentration induced by the presence of surface defects determined by the anodizing and SP processes promotes the occurrence of surface phenomena. In other words, the anodization process induces an increase in the formation of micro-cavities, thus generating localized areas of stress concentration. These stress concentration points have the potential to compromise the fatigue strength of the material, contributing to the formation and propagation of cracks under cyclic loading.

Finally, to further investigate the phenomenon of fatigue crack propagation, an in-depth SEM investigation was performed in regions II and III of the specimens, corresponding respectively to slow and fast crack growth.

This analysis allowed to highlight the incremental growth of cracks under the action of cyclic stresses. To this scope, the distances of the striations (Figure 14) were calculated at the center of regions II and III. It is commonly acknowledged that the growth rate of fatigue cracks da/dN at a specific location within the stable propagation region is obtainable from the distance between fatigue striations. Usually, this distance varies continuously as a result of the variation of the amplitude of the stress intensity factor (SIF) ΔK at the crack tip.

The striation distance values shown in Table 2 are obtained by arithmetically averaging 10 distance values of striations placed within the considered position. A reduction in striation distance is immediately observed in shot peened samples compared to simply machined samples. This reduction indicates slower fatigue crack growth attributable to compressive stresses induced by the peening process. An increase in the striation distance at region III compared to region II due to the increase in the SIF at the crack tip is also noticeable. It is interesting to compare the striation distance at regions II and III between LP + An. and SP + An. samples: In region I, the propagation rate in the two different types of specimens is almost comparable; on the contrary, the striation distance diverges significantly in region II, showing a higher crack propagation speed in the case of LP + An. samples than in SP + An. These findings highlight the importance of addressing and minimizing surface defects with the aim of enhancing the structural integrity and fatigue performance.

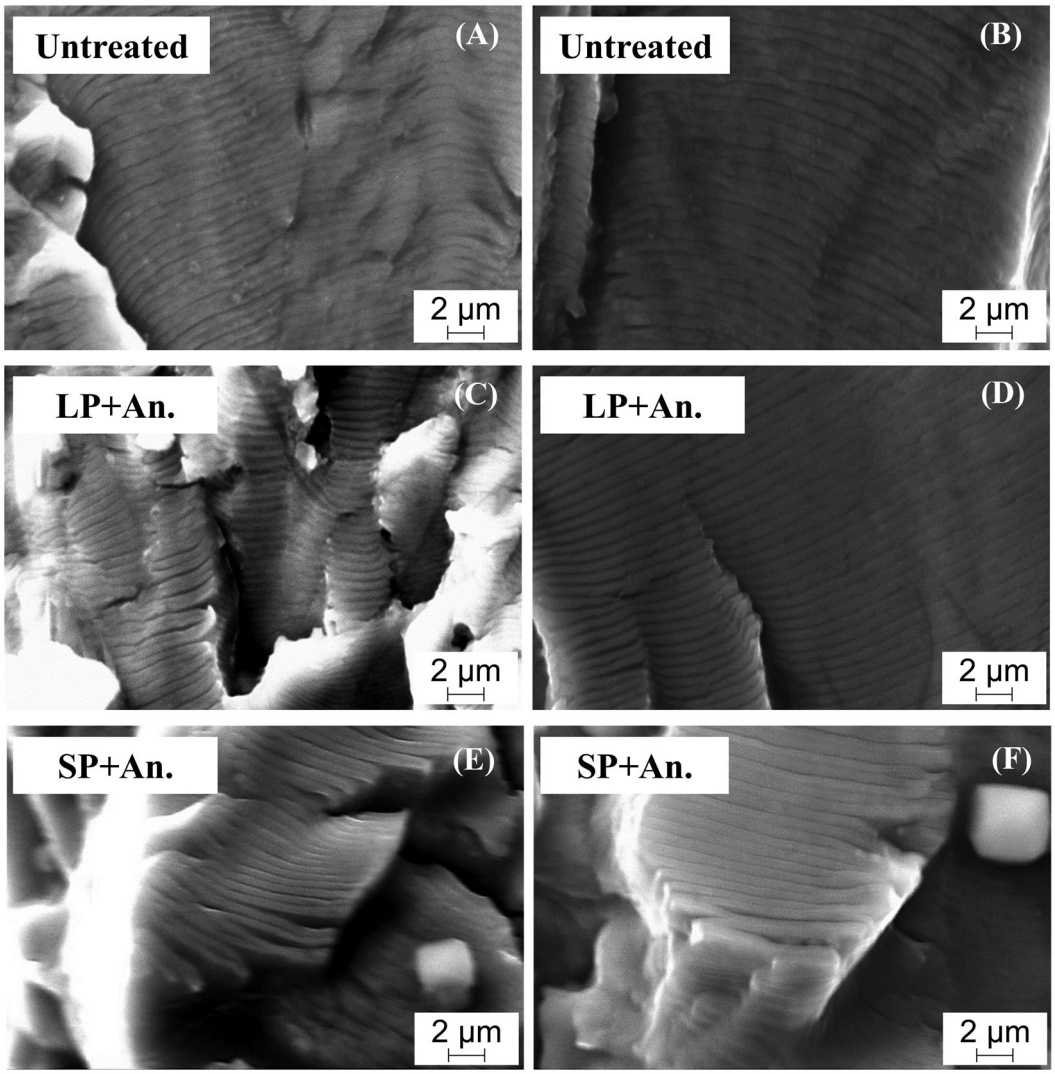

FIGURE 14 Fatigue striation distance in two different positions inside the stable crack propagation region: (A, B) untreated, (C, D) LP + An., and (E, F) SP + An.

TABLE 2 Fatigue striation distances at positions 1 and 2 within the region of stable fatigue crack propagation for the different components analyzed.

	Region II		Region III	
Specimen type	**Distance from crack initiation site (mm)**	**Striation distance (μm)**	**Distance from crack initiation site (mm)**	**Striation distance (μm)**
As M.	3	0.60 ± 0.05	9	0.80 ± 0.09
LP + An.	3	0.43 ± 0.03	9	0.64 ± 0.03
SP + An.	3	0.38 ± 0.05	9	0.47 ± 0.04

4 | CONCLUSIONS

With the aim of testing the possibility of employing SP and LP pre-treatments on specimens subjected to the TSA anodizing process, the following results emerged from the present research:

- The surface morphology of the samples is distinctly and significantly affected by both the simple anodization process and SP and LP treatments.
- The anodic layer followed the intricate details and irregularities of the specimen's surface and is characterized by the presence of numerous micro-voids non-

uniformly distributed, whose size is generally less than 25 μm.

- Although similar in shape and size, the defect density found on the surface of the anodic layer of the LP + An. components turns out to be significantly higher than those measured in the An. and SP + An. specimens due to the different anodizing time to which the specimens of the first group are subjected. Moreover, this difference in anodizing time also resulted in the development of anodic layers of different thicknesses on SP + An. (2 μm) and LP + An. (4 μm) specimens.
- TSA treatment does not induce significant changes of residual stresses compared with the reference values measured on the untreated material. The SP and LP processes, on the other hand, induce a strong uniform compressive state on the examined surface, the intensity of which turns out to be generally less than −200 MPa. Moreover, the LP process induces a stress profile that exhibits a compressive maximum stress of −350 MPa at 0.4 mm from the treated surface and a penetration depth of more than 1 mm.
- TSA anodizing results in a significant reduction in fatigue performance in the HCF region of the *S–N* diagrams due to the preferential nucleation of fatigue cracks at the intrinsic micro-voids in the oxide layer.
- Both SP and LP processes were able to compensate for the reduction in fatigue life caused by the subsequent anodizing treatment.
- Distinctions in fatigue performance are evident between SP + An. and LP + An. specimens. In the LCF regime, the two fatigue curves are almost overlapping, while in the HCF regime, the two curves diverge and the fatigue limit of SP + An. specimens turns out to be higher than that of LP + An. specimens. This phenomenon can likely be related to the higher defect density found in LP + An specimens due to the prolonged duration of the anodizing process.
- Therefore, the results obtained demonstrate the beneficial role of peening as pre-treatments to anodizing on the fatigue performance of 7050 samples. However, a careful assessment of the micro-voids of the anodic layer is absolutely necessary to avoid compromising the material fatigue strength.

NOMENCLATURE

L_0	distance between outer rollers in the four-point bending fatigue setup
L_i	distance between inner rollers in the four-point bending fatigue setup
S_e	fatigue limit at 3 million cycles
σ_x	residual stresses in the *x*-direction
σ_y	residual stresses in the *y*-direction
σ_{UTS}	ultimate tensile strength
σ_{yield}	tensile yield strength
E	Young's modulus
F	axial load
N	number of cycles to failure
R	fatigue stress ratio
S	stress level
υ	Poisson's ratio

ACKNOWLEDGMENTS

The authors would like to thank Airbus Operations GmbH—ZAL Tech Center for providing the material necessary to carry out the activities described in this work.

CONFLICT OF INTEREST STATEMENT

All the authors deny the existence of affiliations or involvements with financial or non-financial purposes in relation to the activities described in this work.

DATA AVAILABILITY STATEMENT

The data that support the findings of this study are available from the corresponding author upon reasonable request.

ORCID

M. A. Attolico https://orcid.org/0000-0001-5956-284X
V. Moramarco https://orcid.org/0000-0003-1955-2166

REFERENCES

1. Liu J-h, Li M, Li S-m, Huang M. Effect of the microstructure of Al 7050-T7451 on anodic oxide formation in sulfuric acid. *Int J Miner Metall*. 2009;16(4):432-438.
2. Hughes AE, Birbilis N, Mol JMC, Garcia SJ, Zhou X, Thompson GE. High strength Al-alloys: microstructure, corrosion and principles of protection. n.d.
3. Martínez-Viademonte MP, Abrahami ST, Hack T, Burchardt M, Terryn H. A review on anodizing of aerospace aluminum alloys for corrosion protection. *Coatings*. 2020;10:1-30.
4. Dhanish S, Yoganandan G, Balaraju JN. Development of TSA anodized/MnVO sealed coating using a statistical approach for Al 7075 alloy and a study of its corrosion behaviour. *Surf Coat Technol*. 2020;402:126316.
5. del Olmo R, Mohedano M, Visser P, Rodriguez A, Matykina E, Arrabal R. Effect of cerium (IV) on thin sulfuric acid anodizing of 2024-T3 alloy. *J Mater Res Technol*. 2021;15:3240-3254.
6. Chanyathunyaroj K, Samit W, Poonthananiwatkul C, Phetchcrai S. Effect of coatings on the mechanical properties and fatigue life of 6061 aluminum alloys. *Trans Indian Inst Met*. 2021;74:2135-2147.
7. de Camargo JAM, Cornelis HJ, Cioffi VMOH, Costa MYP. Coating residual stress effects on fatigue performance of 7050-T7451 aluminum alloy. *Surf Coat Technol*. 2007;201:9448-9455.
8. Minto TA, de Oliveira VMCA, Voorwald HJC. Plasma immersion ion implantation: influence on the rotating bending

fatigue strength of AA 7050-T7451 aluminum alloy. *Int J Fatigue*. 2017;103:17-27.
9. Fares C, Hemmouche L, Belouchrani MA, Amrouche A, Chicot D, Puchi-Cabrera ES. Coupled effects of substrate microstructure and sulphuric acid anodizing on fatigue life of a 2017A aluminum alloy. *Mater Des*. 2015;86:723-734.
10. Savas TP, Earthman JC. Fatigue crack nucleation studies on sulfuric acid anodized 7075-T73 aluminum. *J Mater Eng Perform*. 2014;23:2131-2138.
11. Hemmouche L, Fares C, Belouchrani MA. Influence of heat treatments and anodization on fatigue life of 2017A alloy. *Eng Fail Anal*. 2013;35:554-561.
12. Nie B, Zhang Z, Zhao Z, Zhong Q. Effect of anodizing treatment on the very high cycle fatigue behavior of 2A12-T4 aluminum alloy. *Mater Des*. 2013;50:1005-1010.
13. Lee E, Jeong Y, Kim S. S-N fatigue behavior of anodized 7050-t7451 produced in different electrolytes. *Metall Mater Trans A Phys Metall Mater Sci*. 2012;43:2002-2011.
14. Shahzad M, Chaussumier M, Chieragatti R, Mabru C, Rezai-Aria F. Effect of sealed anodic film on fatigue performance of 2214-T6 aluminum alloy. *Surf Coat Technol*. 2012;206:2733-2739.
15. Chaussumier M, Mabru C, Chieragatti R, Shahzad M. Fatigue life model for 7050 chromic anodized aluminium alloy. *Procedia Eng*. 2013;66:300-312.
16. den Braver-Sewradj SP, van Benthem J, Staal YCM, Ezendam J, Piersma AH, Hessel EVS. Occupational exposure to hexavalent chromium. Part II. Hazard assessment of carcinogenic effects. *Regul Toxicol Pharmacol*. 2021;126:105045.
17. Verdaguer DS. Alternative surface treatments without chromium content in aeronautical aluminium alloys, MSc thesis. 2015.
18. Critchlow GW, Yendall KA, Bahrani D, Quinn A, Andrews F. Strategies for the replacement of chromic acid anodising for the structural bonding of aluminium alloys. *Int J Adhes Adhes*. 2006;26:419-453.
19. Ding Z, Smith BA, Hebert RR, Zhang W, Jaworowski MR. Morphology perspective on chromic acid anodizing replacement by thin film sulfuric acid anodizing. *Surf Coat Technol*. 2018;350:31-39.
20. Museux F, Theilmann R. Introducing more eco-efficient chemical treatments for aircraft structure, towards a chromate-free airbus. FAST45 - Airbus Technical magazine 2009.
21. Okene SU, Abdullahi M, Gana A. Corrosion improvement of AA7075 through precipitation hardness and anodization. *Mater Today Proc*. 2021;38:729-736.
22. Costenaro H, Lanzutti A, Paint Y, et al. Corrosion resistance of 2524 Al alloy anodized in tartaric-sulphuric acid at different voltages and protected with a TEOS-GPTMS hybrid sol-gel coating. *Surf Coat Technol*. 2017;324:438-450.
23. Yoganandan G, Balaraju JN, Manikandanath NT, et al. Surface and electrochemical characteristics of novel chromate-free Mn-V oxyanion sealed tartaric–sulfuric acid anodized coating. *J Mater Eng Perform*. 2018;27:6175-6188.
24. Zhao X, Wei G, Yu Y, Guo Y, Zhang A. An analysis of mechanical properties of anodized aluminum film at high stress. *Surf Rev Lett*. 2015;22:1-7.
25. Attolico MA, Casavola C, Moramarco V, Renna G, Furfari D, Busse DO. Influence of tartaric-sulfuric acid anodic film on four-point bending fatigue behavior of AA 7050-T7451 samples. *Fatigue Fract Eng Mater Struct*. 2022;45:3716-3730.
26. Liu KK, Hill MR. The effects of laser peening and shot peening on fretting fatigue in Ti–6Al–4V coupons. *Tribol Int*. 2009;42:1250-1262.
27. Rodopoulos CA, Romero JS, Curtis SA, De Los Rios ER, Peyre P. Effect of controlled shot peening and laser shock peening on the fatigue performance of 2024-T351 aluminum alloy. 2024.
28. Gao YK. Improvement of fatigue property in 7050-T7451 aluminum alloy by laser peening and shot peening. *Mater Sci Eng A*. 2011;528:3823-3828.
29. Attolico MA, Barile C, Casavola C, Moramarco V, Furfari D, Busse DO. Effects of laser shock peening on surface roughness and residual stress of AA 7050-T7451. *J Mater Eng Perform*. 2022;31:7973-7988.
30. Toparli MB, Fitzpatrick ME. Residual stresses induced by laser peening of thin aluminium plates. *Mater Sci Forum*. 2011;681:504-509.
31. Glaser D, Polese C, Bedekar RD, et al. Laser shock peening on a 6056-T4 aluminium alloy for airframe applications. *Adv Mat Res*. 2014;891–892:974-979.
32. Salimianrizi A, Foroozmehr E, Badrossamay M, Farrokhpour H. Effect of laser shock peening on surface properties and residual stress of Al6061-T6. *Opt Lasers Eng*. 2016;77:112-117.
33. Turski M, Clitheroe S, Evans AD, Rodopoulos C, Hughes DJ, Withers PJ. Engineering the residual stress state and microstructure of stainless steel with mechanical surface treatments. *Appl Phys A Mater Sci Process*. 2010;99:549-556.
34. Kovacı H, Bozkurt YB, Yetim AF, Aslan M, Çelik A. The effect of surface plastic deformation produced by shot peening on corrosion behavior of a low-alloy steel. *Surf Coat Technol*. 2019;360:78-86.
35. Kovacı H, Hacısalihoğlu İ, Yetim AF, Çelik A. Effects of shot peening pre-treatment and plasma nitriding parameters on the structural, mechanical and tribological properties of AISI 4140 low-alloy steel. *Surf Coat Technol*. 2019;358:256-265.
36. Siddaiah A, Mao B, Liao Y, Menezes PL. Surface characterization and tribological performance of laser shock peened steel surfaces. *Surf Coat Technol*. 2018;351:188-197.
37. Maawad E, Brokmeier HG, Wagner L, Sano Y, Genzel C. Investigation on the surface and near-surface characteristics of Ti–2.5 Cu after various mechanical surface treatments. *Surf Coat Technol*. 2011;205:3644-3650.
38. Montross CS, Wei T, Ye L, Clark G, Mai YW. Laser shock processing and its effects on microstructure and properties of metal alloys: a review. *Int J Fatigue*. 2002;24:1021-1036.
39. *ASM Handbook: Properties and Selection: Nonferrous Alloys and Special-Purpose Materials*. ASM Handbook Committee; 1990.
40. British Standards Institution, European Committee for Standardization. BS EN 6072:2010 BSI Standards Publication Aerospace series—metallic materials—test methods—constant amplitude fatigue testing 2010.
41. European Committee for Standardization. EN 15305:2008—non-destructive testing—test method for residual stress analysis by X-ray diffraction. 2008.
42. Lonyuk B, Apachitei I, Duszczyk J. The effect of oxide coatings on fatigue properties of 7475-T6 aluminium alloy. *Surf Coat Technol*. 2007;201:8688-8694.

43. Montross CS, Brandt M, Swain MV. Self-limiting hardness changes in laser peened 6061-T6 aluminium. *Surf Eng*. 2001;17:477-482.
44. Camargo A, Voorwald H. Influence of anodization on the fatigue strength of 7050-T7451 aluminium alloy. *Fatigue Fract Eng Mater Struct*. 2007;30:993-1007.
45. Li N, Li H, Zhou J, Liu H, Liu C, Qu S. Influence of different surface treatments on fatigue life of 7050 Al alloy. *Mater Sci Forum*. 2018;944:142-148. doi:10.4028/www.scientific.net/MSF.944.142
46. Hadzima B, Nový F, Trško L, Pastorek F, Jambor M, Fintová S. Shot peening as a pre-treatment to anodic oxidation coating process of AW 6082 aluminum for fatigue life improvement. *Int J Adv Manuf Technol*. 2017;93:3315-3323.
47. Attolico MA, Casavola C, Cazzato A, Moramarco V, Renna G. Effect of extrusion temperature on fused filament fabrication parts orthotropic behaviour. *Rapid Prototyp J*. 2020;26:639-647.
48. Luong H, Hill MR. The effects of laser peening and shot peening on high cycle fatigue in 7050-T7451 aluminum alloy. *Mater Sci Eng A*. 2010;527:699-707.

SUPPORTING INFORMATION

Additional supporting information can be found online in the Supporting Information section at the end of this article.

How to cite this article: Renna G, Attolico MA, Moramarco V, Casavola C. The role of peening processes as a pre-treatment to anodizing on fatigue behavior of aircraft aluminum alloy. *Fatigue Fract Eng Mater Struct*. 2024;1-19. doi:10.1111/ffe.14231.